INORGANIC CHEMISTRY FRONTIERS

RESEARCH ARTICLE

View Article Online
View Journal | View Issue

Cite this: *Inorg. Chem. Front.*, 2024, **11**, 7966

Design of Dy^{III} single-molecule magnets with molecularly installed luminescent thermometers based on bridging $[Pt^{II}(CN)_2(C^N)]^-$ complexes†

Pawel J. Bonarek, [a] Mikolaj Zychowicz, [a,b] Jan Rzepiela, [a,b] Michal Liberka, [a,b] Sebastian Baś, [a] Jakub J. Zakrzewski *[a,b] and Szymon Chorazy *[a]

Luminescent Single-Molecule Magnets (SMMs) have gained broad scientific attention due to their potential applications in the dual sensing of temperature and magnetic field or optical thermometry for the self-monitoring of temperature in SMM-based devices. We present a route toward thermoresponsive emissive SMMs based on linking two molecular components separately providing luminescent thermometry and SMM features. We combined Dy(III) centers of a rationally constrained coordination sphere giving tunable magnetic anisotropy with an emissive dicyanido(2-phenylpyridinato)platinate(II) anion, $[Pt^{II}(CN)_2(ppy)]^-$ exhibiting ratiometric optical thermometry. These molecular precursors undergo self-assembly into $\{[Dy^{III}(MeOH)_2(NO_3)]_2[Pt^{II}(CN)_2(ppy)]_4\}\cdot n$(solvent) (**1**) coordination chains of a weak field-induced SMM behavior. However, upon the exchange of MeOH molecules, axially aligned within eight-coordinated Dy(III) complexes, by O-donor organic ligands, including 4(1*H*)-pyridone (**2**), pyridazin-4(1*H*)-one (**3**), and *N*-methylpyridin-4(1*H*)-one (**4**), an improvement of the SMM character was achieved. This is accompanied by the tuning of optical thermometry related to temperature-variable excitation and emission spectra of Pt(II) complexes which leads to the best-performance multifunctionality in a 4(1*H*)-pyridone-containing compound. Our work proves that the heterometallic synthetic approach provides a unique class of SMM-based luminescent thermometers where lanthanide-centered magnetism will not be affected by the light employed to monitor the temperature through an optical process occurring in attached cyanido transition metal complexes.

Received 18th September 2024,
Accepted 25th September 2024

DOI: 10.1039/d4qi02373k

rsc.li/frontiers-inorganic

Introduction

Aiming at smart materials for applications in memory devices and spintronics, the development of lanthanide Single-Molecule Magnets (Ln-SMMs) continues, and one may say it has currently reached its "golden era". Since the discovery of high-performance organometallic SMMs,[1–4] the expectations of the scientific community have risen, especially as the demand for ultrafast calculations may imply that liquid nitrogen cooling of molecular magnets for their proper operation will be considered cost-efficient.[5–8] As Ln^{3+} ions offer not only intrinsic magnetic anisotropy resulting from spin–orbit coupling as well as the appropriate crystal field and its symmetry,[9–15] but also possess f–f electronic transitions giving the light emission in the UV-vis-NIR range, their complexes or inorganic solids find applications in optical industry, security, and medical diagnostics.[16–25] Both these physical features, *i.e.*, magnetic and luminescence, combined are promising for constructing bifunctional devices. Therefore, apart from the determination of the electronic structure by fluorescence spectroscopy,[26–28] photoluminescent Ln-SMMs are studied as optical thermometers,[29–34] magnetic field sensors,[32,35,36] photoswitches,[37–39] and pressure indicators.[40] These additional features may facilitate in the future the contactless readout of the magnetic state of a system, while the introduction of chiro-optical effects,[41–43] second-harmonic generation,[44] and other non-optical phenomena,[45,46] further extend the possible range of applications. In the latter case, the appearance of physical cross-effects might also be expected.[47–49]

Several strategies were employed to introduce luminescence functionalities into Ln-SMMs, utilizing various groups of organic ligands or metalloligands, such as

[a]*Faculty of Chemistry, Jagiellonian University, Gronostajowa 2, 30-387 Kraków, Poland. E-mail: simon.chorazy@uj.edu.pl, j.zakrzewski@uj.edu.pl*
[b]*Doctoral School of Exact and Natural Sciences, Jagiellonian University, Łojasiewicza 11, 30-348 Kraków, Poland*

†Electronic supplementary information (ESI) available: Experimental details. TGA. IR spectra. Additional structural views and data. P-XRD patterns. Additional emission and magnetic characteristics. CCDC 2287738–2287741. For ESI and crystallographic data in CIF or other electronic format see DOI: https://doi.org/10.1039/d4qi02373k

polycyanidometallates.[50–62] Among them, anthracene-functionalized phosphates were found to exhibit their intrinsic luminescence when combined with Dy(III) centers instead of sensitizing the emission of a lanthanide origin; however, they additionally introduce the photo-switching property due to the light-induced 4 + 4 cycloaddition.[50–52] The other strategy employs hexafluoroacetylacetonates with supporting organic ligands which can lead to the sensitization of a lanthanide emission, allowing also the introduction of redox activity or chirality.[53–57] For several years, we and others focused on d–f heterometallic assemblies built of Ln^{3+} ions and diamagnetic cyanido transition metal complexes.[58–62] The latter allowed us to separate magnetically anisotropic Ln(III) complexes within the crystal lattice, as well as sensitize their vis-to-NIR emission. Concerning the functional luminescent part of such systems, we studied the optical thermometry effect. We used diverse parameters of the generated luminescence including the ratio between the main emissive components of two lanthanide ions, the detailed pattern of the re-absorption effect of Ho^{3+} ions within the ligand's emission band, the emission lifetime, and the intensities of hot and cold emission bands within the same emissive multiplet of the Ln^{3+} ion.[63–66] The last approach was the most efficient for designing Ln-SMMs whose operational regime overlaps with the working range of thermometry.[66] These strategies greatly contributed to the development of optical thermometers based on Ln-SMMs. However, all the systems, reported since the rise of this research field in 2019, employ absorption and emission properties related to f–f electronic transitions as the origin of the read-out signal used to define the thermometric parameters (Fig. 1). Therefore, both properties, *i.e.*, optical thermometry and the SMM effect, involve the usage of the same paramagnetic Ln(III) center. As a result, one may state, that even such a smart contactless way of monitoring the temperature of a molecular magnet, bears the risk of losing the magnetic memory effect due to the light-induced population of an excited multiplet showing a different magnetism in the ground state that gives the SMM effect.

In these regards, we decided to search for an alternative strategy toward SMM-based luminescent thermometers where both magnetic and optical properties will co-exist at the molecular scale but do not interfere to keep the critical magnetic memory effect undisturbed. Our idea was to combine the Ln(III)-based SMM behavior with thermosensitive photoluminescence originating purely from a strongly light-absorbing and emissive cyanido metal complex. In the resulting material, the light excitation should be focused only on the cyanido complex and no energy transfer to the Ln(III) centers should occur, leaving Ln-SMM characteristics unchanged. To realize this concept, we decided to employ diamagnetic and strongly emissive cyclometalated square planar Pt(II) com-

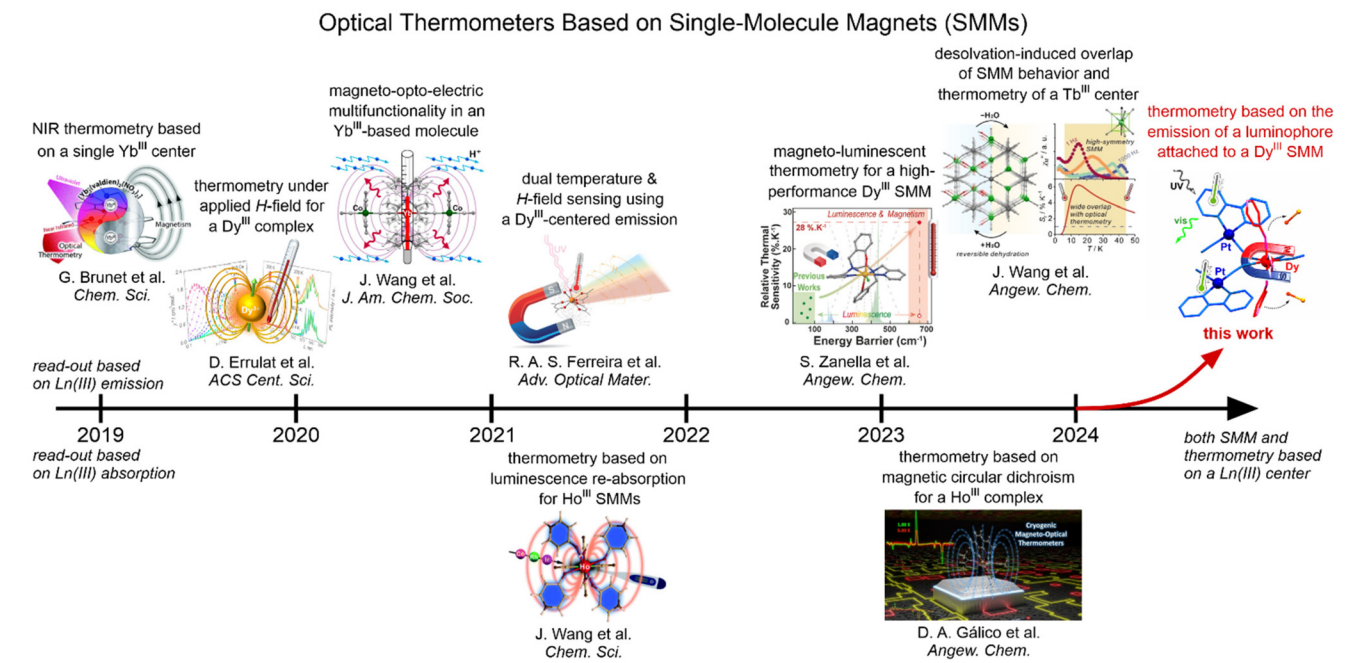

Fig. 1 The timeline of the most crucial achievements in the development of optical thermometry based on SMMs and the research line initialized by this work. The graphic on the top, 1st from the left, has been reproduced from ref. 29 with permission from the Royal Society of Chemistry. The graphic on the top, 2nd from the left, has been adapted from ref. 36, which was published under the ACS AuthorChoice license. The graphic on the top, 3rd from the left, has been adapted with permission from ref. 63. Copyright 2020 American Chemical Society. The graphic on the top, 4th from the left, has been adapted with permission from ref. 32. Copyright 2021 John Wiley & Sons. The graphic on the top, 3rd from the right, has been adapted with permission from ref. 31. Copyright 2023 John Wiley & Sons. The graphic on the top, 2nd from the right, has been adapted with permission from ref. 66. Copyright 2023 John Wiley & Sons. The graphic on the bottom, 1st from the left, has been reproduced from ref. 64 with permission from the Royal Society of Chemistry. The graphic on the bottom, 2nd from the left, has been adapted with permission from ref. 33. Copyright 2023 John Wiley & Sons.

plexes which usually contain a C,N-bidentate (*i.e.*, C^N-type) ligand together with a supporting co-ligand. These complexes were recognized for their efficient and stimuli-responsive visible emission of mixed ligand-centered and metal-to-ligand charge-transfer origin.[67–70] For our purposes, we selected a specific member of this family of complexes, *i.e.*, containing a C,N-bidentate anionic form of 2-phenylpyridine (ppy^-), which provides an emissive character, and two cyanido ligands, which results in the anionic form of the complex making it suitable as a metalloligand for Ln^{3+} ions. This precursor, *cis*-$Pt^{II}(CN)_2(ppy)^-$ was also selected as it is a luminescent analog of recently investigated non-emissive *cis*-dicyanidoiron(II) which was shown to efficiently constrain the Dy(III) coordination sphere within a d–f coordination chain enabling the insertion of two O-donor ligands at the axial positions of the Ln(III) complex which induces the SMM effect.[71] Following these perspectives, we combined magnetically anisotropic Dy^{3+} ions with stimuli-responsive emissive $[Pt^{II}(CN)_2(ppy)]^-$ complexes, obtaining a series of coordination polymers, from initial $\{[Dy^{III}(MeOH)_2(NO_3)]_2[Pt^{II}(CN)_2(ppy)]_4\}\cdot n(solvent)$ (**1**) with MeOH molecules at the axial positions of eight-coordinated Dy(III) complexes to isotopological chains with MeOH molecules exchanged with O-donor ligands, *i.e.*, 4(1*H*)-pyridone (**2**), pyridazin-4(1*H*)-one (**3**), and *N*-methyl-pyridin-4(1*H*)-one (**4**). They combine thermosensitive Pt(II)-centered emission being the basis of ratiometric optical thermometry with Dy(III)-centered SMM features ranging from weak field-induced effect for **1** to its great improvement in **2–4**. The conjunction of luminescence and magnetism, originating from two different metal complexes installed together within a coordination polymer, was tuned by supporting organic ligands affording best-performance multifunctionality for **2**. These effects are discussed based on experimental structural, optical, and magnetic studies, which are supported by *ab initio* calculations.

Results and discussion

Crystals of **1–4** suitable for single-crystal X-ray diffraction (SC-XRD) experiments were obtained by mixing an organic salt of dicyanido(2-phenylpyridinato)platinate(II) with Dy(III) nitrate in the methanol/acetonitrile solution, and diffusion of diethyl ether (see Experimental details in the ESI†). In the absence of additional organic ligands, the crystals of $\{[Dy^{III}(MeOH)_2(NO_3)]_2[Pt^{II}(CN)_2(ppy)]_4\}\cdot 2MeCN\cdot 2.5Et_2O$ (**1**) were obtained (Fig. 2, S1–S3 and Tables S1–S3†). Their structure consists of two symmetry-independent Dy^{III} complexes of the $\{Dy^{III}(MeOH)_2(\mu\text{-}NC)_4(NO_3)\}^{2-}$ formula. According to Continuous Shape Measure (CShM) analysis,[72,73] both of them adopt a dodecahedral geometry. However, in these complexes, one can notice a plane provided by cyanido ligands, which is distorted by a perpendicularly coordinated nitrate anion. Above and below this plane, two coordinated MeOH molecules are positioned, with the related O1–Dy1–O2 and O6–Dy2–O7 angles of 164.0(2)° and 157.7(2)°, respectively. Thus, the Dy(III) coordination geometry resembles a pentagonal bipyramid (Table S3†), proven to be suitable for SMM behavior; however, formally, it is an eight-coordinated complex of a strongly distorted dodecahedral geometry as the equatorially aligned nitrate ion is the O,O-bidentate ligand.[9–13] These Dy(III) complexes are bridged by four $[Pt^{II}(CN)_2(ppy)]^-$ metalloligands into coordination chains of vertex-sharing $\{Dy^{III}_2Pt^{II}_4\}$ squares. To exploit the attractive geometry of Dy^{III} centers, various O-donor ligands were tested to replace axially aligned MeOH ligands. This was achieved using 4(1*H*)-pyridone (4-pyone), pyridazin-4(1*H*)-one (4-pydzone), and *N*-methyl-pyridin-4(1*H*)-one (4-Mepyone).[74] The first case leads to $\{[Dy^{III}(MeOH)(NO_3)(4\text{-pyone})][Dy^{III}(NO_3)(4\text{-pyone})_2][Pt^{II}(CN)_2(ppy)]_4\}\cdot 1.25MeCN\cdot 2MeOH$ (**2**) chains of vertex-sharing squares, similar to **1** (Fig. 2, S1, S2, S4 and Tables S1, S4, S5†). When compared with **1**, both axial MeOH ligands of the Dy^{III} coordination sphere were exchanged only for one Dy^{III} center, (Dy2), while the Dy1 center is coordinated by one MeOH molecule and one 4-pyone ligand. The Dy2 center retains a distorted dodecahedral geometry, while the Dy1 geometry is modified towards a bicapped trigonal prism. However, as for **1**, the similarity to a pentagonal bipyramidal geometry, related to the presence of tightly bonded but formally bidentate nitrate ion, remains for both Dy^{III} complexes (Table S5†), with the axial O–Dy–O angles of 155.6(3)° and 161.5(3)° for Dy1 and Dy2, respectively. An analogous effect was observed for the 4-pydzone ligand giving $\{[Dy^{III}(MeOH)(NO_3)(4\text{-pydzone})][Dy^{III}(NO_3)(4\text{-pydzone})_2][Pt^{II}(CN)_2(ppy)]_4\}\cdot MeCN\cdot 2MeOH\cdot 0.5Et_2O$ (**3**) chains (Fig. 2, S1, S2, S5 and Tables S1, S6, and S7†). The identical results of the CShM analysis, as well as similar O–Dy–O angles of 155.0(3)° and 160.9(3)° for Dy1 and Dy2 centers, respectively, can be ascribed to the similar size of the organic ligand in **2** and **3**. A different behavior was observed for the 4-Mepyone precursor which results in the analogous chains of vertex-sharing squares but with the composition of $\{[Dy^{III}(4\text{-Mepyone})_2(NO_3)]_2[Pt^{II}(CN)_2(ppy)]_4\}\cdot 0.5MeCN\cdot 2MeOH$ (**4**) (Fig. 2, S1, S2, S6 and Tables S1, S8, and S9†). In **4**, both symmetry-independent Dy^{III} centers coordinate two axially aligned 4-Mepyone ligands. Their arrangement is similar to the analogous ligands in **1–3**, with 161.8(9)° and 161.9(11)° O–Dy–O angles for Dy1 and Dy2 centers, respectively. The similarity is also valid for the related coordination geometries as inferred from the CShM analysis showing a dodecahedral shape for both complexes. Some trends can be noticed for Dy–O distances. For nitrate O-atoms, they stay close to 2.4 Å or above for all **1–4** cases, while the O-atoms of MeOH ligands are located in the shorter 2.31–2.35 Å range. For **2** and **3**, supporting organic ligands result in the shorter 2.21–2.29 Å range of the Dy–O distances while, in **4**, the Dy^{III} complexes reveal one shorter (<2.3 Å) and one longer (>2.3 Å) Dy–O bond. This suggests that although a higher degree of MeOH exchange is achieved in **4**, the axiality seems deteriorated due to the steric hindrances and supramolecular interactions. The phase purity and identity of bulk samples of **1–4** along with their structural models were confirmed using a powder X-ray diffraction method (Fig. S7†). This method was also used to prove the isostructurality of **1–4**

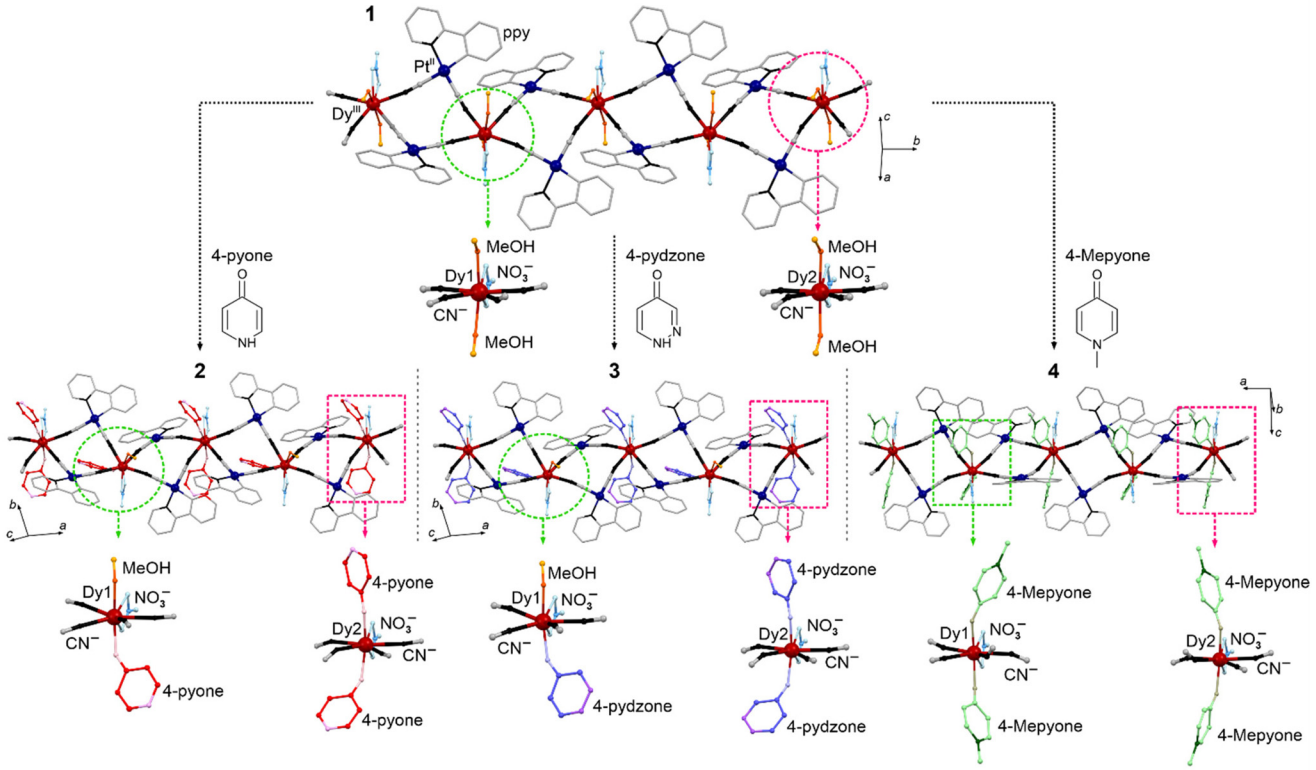

Fig. 2 Visualization of the functionalization of **1** by O-donor organic ligands depicted by the representative views of **1–4**. For each system, the fragment of the $\{Dy_2^{III}Pt_4^{II}\}_n$ chain is presented with insights into the two types of Dy^{III} complexes. The ppy ligands are drawn using sticks (grey and black fragments for C and N atoms, respectively), dark blue balls represent Pt^{II} centers, dark red balls stand for Dy^{III} centers, small cyan balls represent nitrate ions (N – darker hue, O – lighter hue), whereas colors close to orange, red, blue-violet, and green were used for MeOH (C – dark orange, O – light orange), 4-pyone (C – red, O – light pink, N – pink), 4-pydzone (C – blue, O – light blue, N – violet), and 4-Mepyone (C – light green, O – light olive green, N – dark green), respectively.

with their magnetically Y^{III}-diluted samples of **1md–4md** which were prepared for magnetic studies (see Experimental details in the ESI†). All compounds were studied in the mother solution or other protectants as they undergo solvent exchange upon exposition to the air.

Due to the presence of $[Pt^{II}(CN)_2(ppy)]^-$ complexes, which are known to reveal charge transfer (CT) electronic transitions,[67–70] **1–4** show strong broadband light absorption ranging from the UV region to *ca.* 400 nm (Fig. S8†). It is accompanied by residual visible light absorption related to forbidden f–f electronic transitions of Dy^{III} centers. Upon the UV excitation at room temperature, compounds **1–4** exhibit green emission assignable to the CT and (admixed) ligand-centered (LC) excited states of Pt^{II} complexes as typical broad bands with the vibronic structure and nearly-μs emission lifetimes were found (Fig. 3, S9–S17 and Tables S10, S11†).[67–70] In particular, the broad emission bands range from *ca.* 460 to 700 nm, and a few distinct components at *ca.* 485, 515, 545, and 590 were observed. Their positions are similar in **1–4** but the relative intensities of emission components vary between compounds (Fig. 3 and S14–S17†). These differences can be attributed to modified phonon mode schemes which affect the intensities of vibronic components of the CT/LC emission, being governed by the structural variation within the Dy^{III}–Pt^{II} chains and changes in intermolecular interactions and solvent content in the series of **1–4**. Room-temperature emission lifetimes are close to 1 μs in all compounds and rather invariant on the emission maximum. This confirms a single origin of the whole emission as typical for cyclometalated Pt(II) and Ir(III) complexes.[75–80] Upon cooling, the increase of emission lifetimes to *ca.* 21–23 μs at 77 K is observed, thanks to the weakening of emission quenching through thermally-activated vibrations (Fig. S9–S12 and Table S10†). The emission quantum yields (Φ) were determined using a direct method at room temperature (Fig. S13 and Table S10†).[81] The highest Φ value was found for **4**, *i.e.*, 11.0(2)% for the optimal excitation, λ_{exc} of 350 nm; a slightly lower value of 9.6(7)% is registered for **1**, under the same λ_{exc}, while **2** and **3** are characterized by less than halves of these values.

The observed variation in emission quantum yields can be discussed in the context of the role of the MeOH-to-ligand exchange that happens along the series of **1–4**. In general, the exchange of MeOH-to-4-Mepyone in **4** seems to support the emission efficiency which can be assigned to the reduction of vibrations quenching the emission (assuming that the solvent

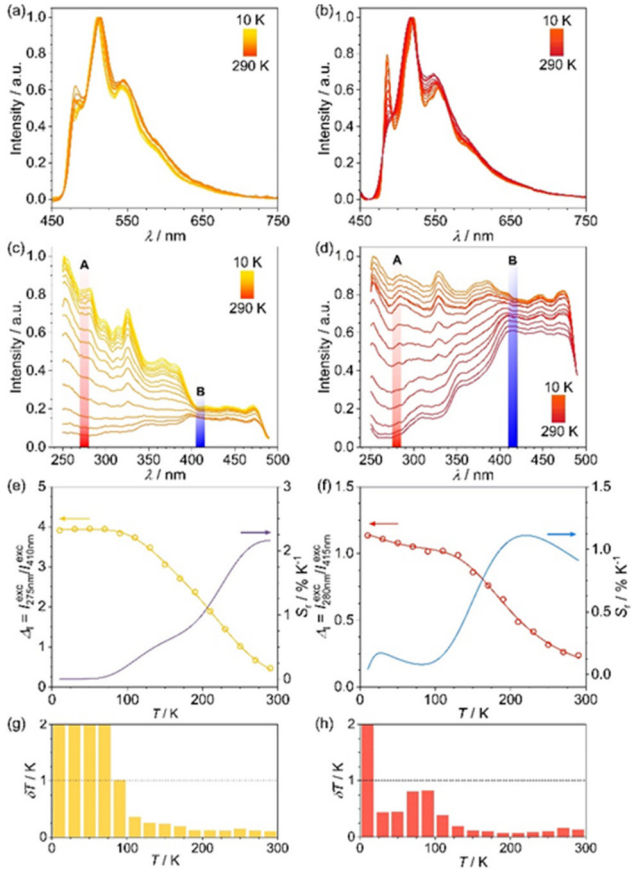

Fig. 3 Temperature-variable emission spectra for **1** (a) and **2** (b) under the 320 nm or 410 nm excitation, respectively; *T*-variable excitation spectra for **1** (c) and **2** (d) at the monitored emission at 510 nm or 515 nm, respectively; *T*-dependences of the thermometric parameter, Δ_I defined as the ratio between integrated areas centered at 275 nm and 410 nm for **1** (e) or 280 nm and 415 nm for **2** (f), together with the relative thermal sensitivity curves, $S_r(T)$, and temperature uncertainties, δT at the indicated temperatures for **1** (g) and **2** (h).

MeOH molecule, involved in the H-bonding network that also includes the emissive Pt(II) complexes, is at least partially responsible for the emission quenching). As a result, the quantum yield for **4** is better than that in the starting material of **1**. On the other hand, the ligands (4-pyone and 4-pydzone) replacing the MeOH molecules in **2** and **3** seem to contribute to the emission quenching more significantly than the solvent which can be related to their involvement in the H-bonding network that also employs the emissive Pt(II) complexes. As a result, their QYs are much lower than those of **1** and **4**. It is important to note that the MeOH-to-ligand exchange is presumably not the only factor that contributes to the variation in QYs in the presented series of compounds as, *e.g.*, diverse non-coordinated solvent contents were observed in **1–4**, thus various additional emission quenching pathways can operate for the obtained systems.

The Dy^{III}-centered emission, expected in the vis-to-NIR range was not observed in **1–4** indicating the lack of direct f–f excitation due to the dominant UV-light absorption by Pt(II) complexes and a lack of the energy transfer to Ln^{3+} ions.[16–18,58–62] Despite this, upon cooling, both the emission and excitation patterns were significantly modulated (Fig. 3, S14–S17 and Table S11†). As the CT/LC emission with the vibronic structure is tuned, the related changes should be correlated with the modification of phonon modes resulting in a different population of critical vibrational states. As a result, emission components change their intensities differently upon cooling while the shifts of the related emission energies are subtle.

More pronounced thermal changes are visible within the excitation patterns. The broad excitation bands located at the edge of the vis-region are weakly amended by temperature. In contrast, for the higher-energy excitation, a large increase in the signal intensity appears on cooling, especially for **1** and **2** (Fig. 3c and d). Such behavior is challenging to elucidate fully but can be related to the cooling-induced favoring of high-energy excitation enhanced due to the weakening of vibrations which hampers the energy relaxation to the emissive state from very high-lying states.

The temperature changes in emission and excitation spectra in **1–4** were tested as a source of ratiometric optical thermometry. Firstly, the numerous combinations of emission/excitation wavelengths were analyzed considering the change in the intensity ratio between high and low temperatures (see the ESI† for details). Then, for the optimal wavelengths, the ranges for integrating the intensities were established to decrease the impact of the experimental noise on the temperature uncertainties of a resulting thermometer. Finally, the thermometric parameters for the whole *T*-range were calculated as the ratio between the integrated areas, eqn (1):

$$\Delta_I = I_A^{area}/I_B^{area}. \quad (1)$$

The *T*-dependence of Δ_I was fitted according to the Mott–Seitz model using either one or two exponential components; then,[82,83] relative thermal sensitivity curves were determined using eqn (2):

$$S_r = \frac{1}{\Delta_I}\left|\frac{\partial \Delta_I}{\partial T}\right|. \quad (2)$$

Furthermore, the temperature uncertainty at a given temperature was evaluated using square roots of sums of squares of intensity uncertainties and calculating the related $\delta\Delta_I$ values (see the ESI†). Only for **2**, it was possible to extract a reasonable calibration curve for the thermometric behavior based on the ratio between integrated areas of emission bands, *i.e.*, using those centered at 485 nm and 502 nm (Fig. S15†). Even then, the maximal S_r value of 0.64% K^{-1} stays below the boundary for the good-performance thermometry (S_r > 1% K^{-1}). However, a reasonable sensitivity was achieved in the 50–220 K range, where S_r > 0.3% K^{-1} and the temperature uncertainty, δT, stays below 1 K. On the other hand, when employing the Δ_I parameters based on excitation spectra, the thermometric performance of all systems is improved (Fig. 3, S14–S17 and Table S11†). Although in each case differently

positioned integrated areas are used, for every such defined $\delta\Delta_I$ parameter the denominator corresponds to the weakly T-dependent excitation at higher λ values, while the higher energy excitation region is used for the numerator of Δ_I parameter. In this approach, the thermometric curves reveal higher thermal sensitivity close to room temperature. The weakest temperature variability within the excitation spectra is found for **4**, which can be noticed by small S_r values below 0.3% K^{-1} (Fig. S17†). For **1** and **3**, the highest sensitivity, of 2.16% K^{-1} and 1.52% K^{-1}, respectively, was reached at 290 K (Fig. S14 and S16†). However, upon cooling, S_r successively decreased, crossing the 1% K^{-1} limit at 200 and 270 K, respectively. A slightly shifted working T-regime is found for **2**, where the maximal S_r of 1.11% K^{-1} appears at 220 K (Fig. 3 and S15†). Then, good thermometric performance is achieved in the 185–265 K range. However, by combining both low-T (emission-based) and high-T (excitation-based) optical thermometry, **2** covers the largest range of temperatures.

Motivated by the geometry of Dy(III) complexes with axially-positioned O-donor ligands in **1–4**, all materials were studied from the viewpoints of direct-current (dc) and alternate-current (ac) magnetic properties. As expected for systems with Ln(III) centers separated by diamagnetic polycyanidometallates, upon cooling to 1.8 K, no sign of magnetic coupling is observed (Fig. S18†). Both the $\chi_M T(T)$ and $M(H)$ curves correspond to the paramagnetism of uncoupled Dy^{III} complexes.[53–66] The detected continuous decrease of the $\chi_M T$ product upon cooling is due to the depopulation of the excited m_J levels within the ground multiplets of the Dy^{III} centers. Within the $M(H)$ curves gathered at 1.8 K, the magnetization reaches *ca.* $10\mu_B$ at 70 kOe without saturation, which is consistent with the presence of two isolated Dy^{III} ions per formula unit in **1–4**.

Similar results of dc magnetic characterization are found for the related magnetically diluted samples **1md–4md** when scaled by the percentage of paramagnetic ions within the sample. Moreover, the $M(H)$ curves at 1.8 K for **2** and **4**, and their diluted analogs, show a hysteretic behavior of the butterfly shape, which is characteristic of the SMM behavior with a zero-field quantum tunneling of the magnetization (QTM) effect; therefore, proving the presence of significant magnetic anisotropy of related Dy^{III} centers (Fig. 4 and S19†). To discuss the crucial crystal-field effect illustrated by the dc magnetism, the *ab initio* calculations of a CASSCF/RASSI/SINGLE_ANISO type were performed.[84–90] They were done within the OpenMolcas package, starting from the experimental geometries of Dy^{III} complexes in **1–3** (Fig. 4, S18, S20–S22 and Tables S12–S15, and details are provided in the ESI†). Related calculations for the crystal structure of **4** were also performed. However, due to the significant structural disorder affecting the reliability of the related structural model, they are excluded from the main discussion, even though they are qualitatively comparable with the results for other compounds (see Table S20 and Fig. S48†, and the related comment in the ESI†).

The considered structural fragments together for **1–3** with the calculated main easy axes of the pseudo-g-tensor are

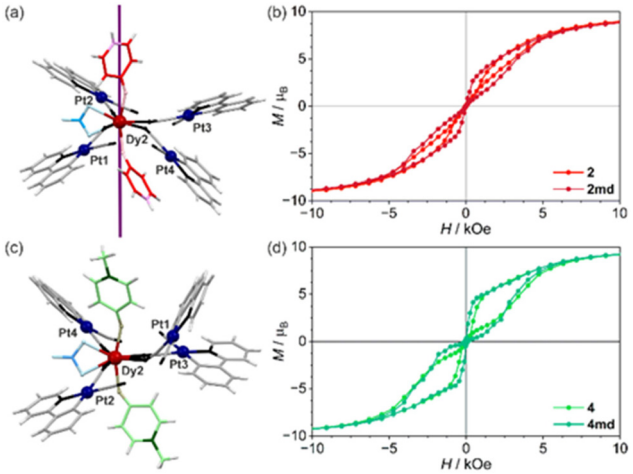

Fig. 4 The alignment of magnetic easy axes for Dy2 centers in **2** (a) and the related arrangement of crucial O-donor ligands in **4** (c) (for the analogous views for other Dy complexes of **1–4**, see Fig. S20–S23†), and the related magnetic hysteresis loops gathered at 1.8 K for the powder samples of **2** and **2md** (b) as well as **4** and **4md** (d).

shown in Fig. 4 and S20–S22.† Two different sizes of the molecular fragments involving each Dy(III) center of the reported compounds were taken into account, *i.e.*, the smaller one with only the nearest ligands around the Dy(III) center (model **S**) and the bigger one with the Dy(III) complex and Pt(II) metalloligands (model **B**, see the ESI† for more details). The results of calculations performed for these two models, **S** and **B**, were very different, both in the obtained energy splitting, composition of m_J levels, and the alignment of magnetic axes. The more accurate data, especially in the context of the reliability of the representative molecular fragment that should involve as many atoms around the Ln(III) center as possible, can be undoubtedly assigned to the calculations for models of a **B**-type; thus, the results for such size of the calculated fragments were used to analyze the ac data for **1–3** (Tables S17–S19†). Using these computational results, the dc magnetic curves could be well-reproduced (Fig. S18†). In **1**, as expected, there is no obvious correlation between the ligands around the Dy(III) centers and the direction of easy magnetic axes which is not surprising as there are no axially aligned organic ligands that can control the magnetic axiality. On the other hand, in **2**, it was found possible to determine the expected direction of the axis for one of the complexes (Dy2 center, Fig. 4a and S21†) indicating that added O-donor ligands of 4-pyone can indeed control the Dy^{III} anisotropy. The second metal center, Dy1, behaves differently which is understandable as there is only a single 4-pyone ligand coordinated to the lanthanide center. Somewhat surprisingly, the calculations indicate that in **3** the center responsible for the SMM performance is Dy1 rather than Dy2, despite the latter being coordinated by two O-donor (4-pydzone) ligands, as the former exhibits higher anisotropy, purity of states, and a larger energy barrier (Table S15†). Nevertheless, such a result stays in line with the experimental data, as the related properties of **3** are closer to those found for

compound **1** which does not possess additional O-donor ligands at the axial positions of the Dy(III) complexes (Fig. 1). At the same time, **3** shows a significantly weaker SMM performance than **2** and **4** bearing axially aligned 4-pyone and 4-Mepyone ligands, respectively, the fact that holds also for the magnetically diluted counterparts. This means the 4-pydzone ligand does not work efficiently enough to control the magnetic axiality of the compound.

The experimental ac magnetic data for **1–4** were collected within field- and temperature-variable curves (Fig. 5 and S23–S47†). In **1**, at the zero dc field, only the onset of the SMM behavior is recorded due to the weak field of two axial MeOH molecules in its Dy^{III} complexes (Fig. S23†). To slow down relaxation times, the H_{dc} field was applied at 1.8 K, resulting in the appearance of $\chi''_M(\nu)$ maxima. From field-variable ac data, two relaxation times (τ) were extracted, with one of them being temperature-independent.[71,91,92] When analyzing the resulting $\tau(T, H)$ dependences, the selected components of eqn (3) were used (see the ESI† for details):

$$\tau^{-1}(H,T) = \tau_0 \exp\left(\frac{-\Delta E}{k_B T}\right) + AH^n T + \frac{B_1}{(1+B_2H^2)} + \left(\frac{1+aH^2}{1+bH^2}\right)CT^N \quad (3)$$

where the subsequent terms correspond to Orbach, direct, QTM, and Raman relaxation effects.[71,91–94] Thus, the second relaxation in **1** was fitted using the contributions from the Raman relaxation and QTM (Fig. S24–S26†). For **1md**, the onset of magnetic relaxation at 0 dc field disappears, suggesting a role of weak magnetic interactions in **1** (Fig. S27†). Field-induced SMM behavior in **1md** can be described as two relaxation processes which is due to the presence of two symmetry-independent Dy centers. For this case, as well as in **1**, the Orbach relaxation was excluded, which is supported by the *ab initio* calculations, showing too large gaps between the Kramers doublets of *ca.* 99 and 63 cm^{-1}, for Dy1 and Dy2 centers, respectively (Tables 1 and S16†).

The MeOH exchange affects the magnetism as suggested by the presence of $M(H)$ hysteresis loops in **2** and **4** (Fig. 4). For them, the presence of slow magnetic relaxation at the zero dc field was noticed and followed in the T-regimes of 2–26 K and 2–24 K, respectively (Fig. 5, S30–S32, S42–S44 and Tables S17, S19†). For **3**, the slow magnetic relaxation at the zero dc field is visible only at the edge of the measurement range (Fig. 5, S36 and Table S18†), presumably due to the increased QTM. A much smaller impact of the QTM is found for **2** but, for the number of T values, the $\chi''_M(\nu)$ maxima remained unaffected. Even a smaller impact of QTM was found for **4**, where the $\chi''_M(\nu)$ maxima quickly moved with the temperature. The

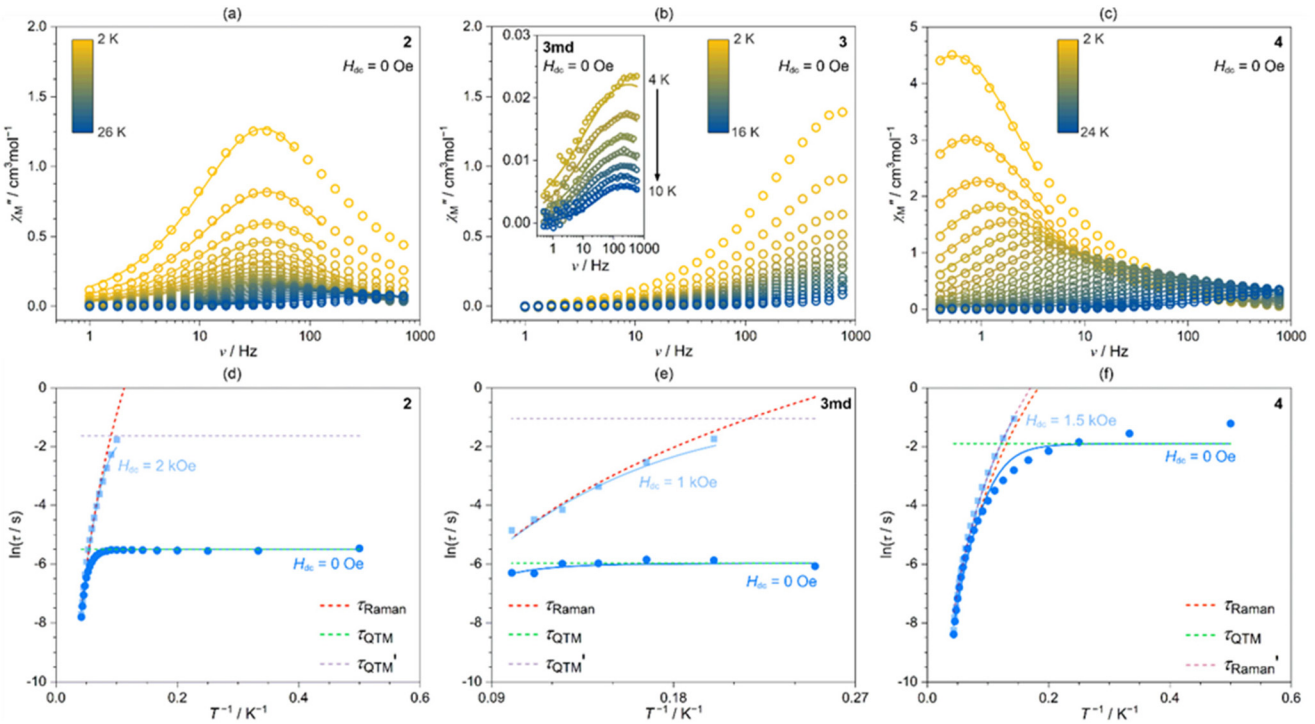

Fig. 5 Alternate-current (ac) magnetic properties of **2**, **3**, **3md**, and **4**, including zero-dc-field frequency dependences of the out-of-phase susceptibility, $\chi''_M(\nu)$, collected in the 2–26 K range for **2** (a), 2–16 K for **3** (b), 2–24 K for **4** (c), and 4–10 K for **3md** (b, inset); T-dependences of the relaxation times under the zero field and the indicated H_{dc} for **2** (d), **3md** (e), and **4** (f). Solid lines in (a–c) represent the best-fit curves obtained using a generalized Debye model. In (d–f), solid lines represent the best-fit curves of the T-dependences of relaxation times, while the individual relaxation routes (Raman and QTM; QTM′ corresponds to the non-zero H_{dc}) are marked by colored dashed lines. The detailed ac magnetic data for **1–4** and **1md–4md**, are gathered in Fig. S23–S47† and Tables 1, S16–S19.†

Table 1 Selected best-fit parameters of the set of the ac magnetic data for **1–4** and their magnetically diluted phases, **1md–4md** (eqn (3))

Compound	**1** [**1md**] (Fig. S23–S29†)	**2** [**2md**] (Fig. 5a, d and S30–S35†)	**3** [**3md**] (Fig. 5b, e and S36–S41†)	**4** [**4md**] (Fig. 5c, f and S42–S47†)
χ''_M maxima at H_{dc} = 0 Oe (2 K, 1–1000 Hz)	No [no]	Yes [yes]	No [yes]	Yes [yes]
B_1/s^{-1}	$2.0(3) \times 10^2$ [$6(1) \times 10^3$]	$2.44(6) \times 10^2$ [$2.8(2) \times 10^1$]	$7.8(7) \times 10^7$ [$3.9(3) \times 10^2$]	6.7(7) [3.0(3)]
B_2/Oe^{-2}	$1.1(2) \times 10^{-6}$ [$4.0(2) \times 10^{-6}$]	$1.1(2) \times 10^{-5}$ [$2.1(6) \times 10^{-6}$]	3.9(4) [$1.5(3) \times 10^{-4}$]	$3(9) \times 10^{-5}$ [0, fixed]
$C/s^{-1}\ K^{-N}$	$2.1(2) \times 10^{-3}$ [$2.5(5) \times 10^1$]	$7.2(2) \times 10^{-8}$ [$6.8(2) \times 10^{-8}$]	$1.43(5) \times 10^{-5}$ [$1.0(2) \times 10^{-3}$]	$7.0(2) \times 10^{-3}$ [$2.22(5) \times 10^{-5}$]
a, b/Oe^{-2}	—	—	—	$1.50(7) \times 10^{-5}$, $2.3(1) \times 10^{-5}$ [$1.62(5) \times 10^{-5}$, 2.27×10^{-5}]
N	6.38(8) [4.77(2)]	7.529(9) [7.24(2)]	6.35(2) [5.24(2)]	5.63(1) [5.964(8)]
$A/s^{-1}\ K^{-n}$	–[$4.27(6) \times 10^{-9}$]	—	—	–[$4.8(17) \times 10^{-16}$]
n	–[3.46(2)]	—	—	–[4 (fixed)]

application of the external field, both for **2** and **4**, reduced QTM, without introducing a field-induced direct process. Then, under the elevated field, the Raman relaxation was fully uncovered. Although several attempts were made to fit the *T*-variable ac data by employing the Orbach relaxation, the related energy barrier values were found to be unreliable. Therefore, this process was removed from the consideration, and the data were fitted using Raman relaxation and QTM. In the case of **3**, the application of the external field partially quenches QTM leading to longer relaxation times. However, at the more elevated H_{dc} values, the direct process is activated and the relaxation time is again shortened. Such behavior leads to an optimal field of 2 kOe, which was employed to study the field-induced SMM effect in **3** (Fig. S37 and S38†). The obtained *T*-dependence can be fitted again by employing the terms of Raman and QTM. Similar results were found after magnetic dilution. For **3md** (Fig. S39–S41†), the smaller content of Dy^{III} centers and the related removal of the residual magnetic interactions gave the detectable τ values at zero dc field. The crucial parameters of slow magnetic relaxation in **1–4** are collected in Table 1.

For **2–4**, only a single magnetic relaxation process can be distinguished. Such an effect suggests that only centers with two O-donor aromatic ligands are involved in the SMM behavior. For **2** and **3**, the Dy^{III} center coordinating a single supporting organic ligand seems to reveal worse anisotropy than those of **1** (Tables 1 and S13–S15†). In **4**, the rationalization of the SMM behavior can be delivered by the analogy to the other systems bearing Dy centers with two O-donor organic ligands. This statement is supported by the lack of the Orbach relaxation for **4** and **4md**. Within the series, the highest purity of the ground Kramers doublet is found in **2** (Dy2, Table S14†), and the related transversal pseudo-*g*-tensor components are near zero. For **4**, the fact of an even smaller impact of the QTM suggests even higher ground state purity for at least one of the Dy centers. However, significant structural changes are present between Dy1 and Dy2 centers in **4**, which together with the occurrence of only one relaxation time within the ac data, suggests a much weaker anisotropy for one of them. Both centers are rather similar in the context of the Dy–O(organic ligand) and Dy–N(cyanido ligand) distances, O–Dy–O angle, and matching the same geometry determined from the CShM analysis (Tables S8 and S9†). However, in the case of the Dy2 center, a slightly elongated Dy–O distance for the coordinated nitrate anion of over 2.5 Å may be the source of an increased anisotropy by approaching a lower coordination number of seven, known for its good SMM performance. Apart from the reduced impact of QTM in **4**, a smaller *N* of the Raman relaxation was detected, giving rise to more pronounced *M*(*H*) hysteresis at 1.8 K. Moreover, only for **4**, it was crucial to employ the *H*-dependent form of the Raman relaxation, which stems from the predominance of this relaxation both in the zero dc field and under its higher values (Table S19†).[93,94]

A similar behavior to **2** and **4**, was observed for the **2md** and **4md** analogs (Fig. S33–S35, S45–S47† and Tables 1, S17, S19†); thus, the difference in the QTM should not be linked

with residual magnetic interactions but with the ground state purity. In these regards, the positive effect of the MeOH exchange upon Dy^{III} magnetic anisotropy is observed in both the *ab initio* analysis and the experiment. Interestingly, for **1**, relatively large energy gaps were calculated between the ground and the first excited doublet of 99 and 63 cm^{-1}. Despite this, a weak field induced by MeOH molecules results in highly mixed ground Kramers doublets, facilitating the QTM. A similar case was observed for **3**, showing only the onset of field-free SMM behavior while the ground state purity allowed us to observe a good SMM effect in compound **2**.

Conclusions

We report a family of photoluminescent single-molecule magnets, obtained using a rational design of the crystal field around Dy(III) centers based on their incorporation into heterometallic coordination polymers with dicyanido(2-phenyl-pyridinato)platinate(II) anions (see the additional comment on the concept of SMM-based coordination polymers in the ESI†), with the further support of O-donor organic ligands placed at the axial positions of eight-coordinated lanthanide complexes of strongly distorted dodecahedral or bicapped trigonal prism geometries. Strongly UV-light-absorbing Pt(II) molecular units serve as the only luminophores providing the visible emission of the mixed charge transfer (CT) and ligand-centered (LC) character in the broad temperature range. The Dy(III) emission remains inactive due to the lack of energy transfer between Pt (II) CT/LC states toward Dy(III) centers and the negligible role of direct f–f excitation. As a result, the optical properties are exclusively related to the Pt(II) complexes while the magnetic ones are due to the nature of Dy(III) centers. We studied *T*-variable luminescence characteristics finding the thermometric behavior, especially well-pronounced for the excitation spectra for the CT/LC emission of Pt(II)-cyanido units in compounds bearing only MeOH molecules and those supported by 4(1*H*)-pyridone ligands. Obtained compounds reveal tunable SMM features generated by inducing the proper geometry of Dy(III) centers, constrained by cyanido ligands, and the axial alignment of supporting O-donor ligands. The exchange of MeOH molecules, which serve as axial ligands for the pristine system, with O-donor organic ligands improves the magnetic anisotropy of Dy(III) centers, leading to the magnetic hysteresis loop for systems with 4(1*H*)-pyridone and *N*-methyl-pyridin-4 (1*H*)-one. The employed strategy for the SMM construction can be further explored by testing other types of organic ligands, in the best scenario with more negatively charged donor atoms, which can be conveniently placed at the axial positions of the Dy(III) complexes within the proposed coordination skeleton. Considering the reported compounds, the system based on 4(1*H*)-pyridone exhibits the best-performance equilibrium between two functionalities, *i.e.*, the SMM effect and ratiometric optical thermometry. Moreover, depending on the optical features employed, the latter effect was found to work both in the cryogenic and near-room temperature range. As the most important outcome, we proved that it is possible to apply a heterometallic synthetic approach for designing the SMM-based optical thermometer for which the optical response is not connected with the property of lanthanide centers, thus leaving their SMM characteristics unaffected. This is the route to monitor the temperature of SMM-based electromagnetic devices without influencing the magnetic memory effect, thus overcoming the technical issue appearing for SMM-based optical thermometers employing a single Ln (III) center for both magnetic and optical effects (Fig. 1).[29–36,63–66] The presented route is worth further exploration by searching for novel thermoresponsive luminophores that can be molecularly attached to high-performance lanthanide single-molecule magnets. This is expected to address the upcoming challenges within the fruitful usage of the reported concept, which include the generation of both good SMM behavior and good-performance luminescent thermometry in the same temperature range as well as further observation of the synergistic effect between the magnetic and optical effects incorporated into such advanced magneto-luminescent molecular systems.

Data availability

The data supporting this article have been included as part of the ESI.† Crystallographic data for **1**, **2**, **3**, and **4** have been deposited at the CCDC database under 2287738, 2287739, 2287740, and 2287741 numbers.† The other data can be obtained from the corresponding author.

Conflicts of interest

There are no conflicts to declare.

Acknowledgements

This work was financed by the National Science Centre of Poland, the OPUS-21 project, no. 2021/41/B/ST5/02544. The research has been supported by an infrastructure grant from the Faculty of Chemistry under the Strategic Programme Excellence Initiative at Jagiellonian Univ. The study was carried out using the research infrastructure co-funded by the EU in the framework of the Smart Growth Operational Program, Measure 4.2; Grant No. POIR.04.02.00-00-D001/20, "ATOMIN 2.0 – ATOMic scale science for the INnovative economy". We also gratefully acknowledge Polish high-performance computing infrastructure PLGrid (HPC Center: ACK Cyfronet AGH) for providing computer facilities and support within computational grant no. PLG/2019/013095.

References

1 C. A. P. Goodwin, F. Ortu, D. Reta, N. F. Chilton and D. P. Mills, Molecular magnetic hysteresis at 60 kelvin in dysprosocenium, *Nature*, 2017, **548**, 439–442.
2 F.-S. Guo, B. M. Day, Y.-C. Chen, M.-L. Tong, A. Mansikkamäki and R. A. Layfield, A Dysprosium Metallocene Single-Molecule Magnet Functioning at the Axial Limit, *Angew. Chem., Int. Ed.*, 2017, **56**, 11445–11449.
3 F.-S. Guo, B. M. Day, Y.-C. Chen, M.-L. Tong, A. Mansikkamäki and R. A. Layfield, Magnetic hysteresis up to 80 kelvin in a dysprosium metallocene single-molecule magnet, *Science*, 2018, **362**, 1400–1403.
4 C. A. Gould, K. R. McClain, D. Reta, J. G. C. Kragskow, D. A. Marchiori, E. Lachman, E.-S. Choi, J. G. Analytis, R. D. Britt, N. F. Chilton, B. G. Harvey and J. R. Long, Ultrahard magnetism from mixed-valence dilanthanide complexes with metal-metal bonding, *Science*, 2022, **375**, 198–202.
5 D. N. Woodruff, R. E. P. Winpenny and R. A. Layfield, Lanthanide single-molecule magnets, *Chem. Rev.*, 2013, **113**, 5110–5148.
6 V. Vieru, S. Gomez-Coca, E. Ruiz and L. F. Chibotaru, Increasing the Magnetic Blocking Temperature of Single-Molecule Magnets, *Angew. Chem., Int. Ed.*, 2023, **63**, e202303146.
7 L. Bogani and W. Wernsdorfer, Molecular spintronics using single-molecule magnets, *Nat. Mater.*, 2008, **7**, 179–186.
8 E. Coronado, Molecular magnetism: from chemical design to spin control in molecules, materials and devices, *Nat. Rev. Mater.*, 2020, **5**, 87–104.
9 N. Ishikawa, M. Sugita, T. Ishikawa, S. Koshihara and Y. Kaizu, Lanthanide Double-Decker Complexes Functioning as Magnets at the Single-Molecular Level, *J. Am. Chem. Soc.*, 2003, **125**, 8694–8695.
10 Y.-C. Chen, J.-L. Liu, L. Ungur, J. Liu, Q.-W. Li, L.-F. Wang, Z.-P. Ni, L. F. Chibotaru, X.-M. Chen and M.-L. Tong, Symmetry-Supported Magnetic Blocking at 20 K in Pentagonal Bipyramidal Dy(III) Single-Ion Magnets, *J. Am. Chem. Soc.*, 2016, **138**, 2829–2837.
11 J. Liu, Y.-C. Chen, J.-L. Liu, V. Vieru, L. Ungur, J.-H. Jia, L. F. Chibotaru, Y. Lan, W. Wernsdorfer, S. Gao, X.-M. Chen and M.-L. Tong, A Stable Pentagonal Bipyramidal Dy(III) Single-Ion Magnet with a Record Magnetization Reversal Barrier over 1000 K, *J. Am. Chem. Soc.*, 2016, **138**, 5441–5450.
12 J.-L. Liu, Y.-C. Chen and M.-L. Tong, Symmetry strategies for high performance lanthanide-based single-molecule magnets, *Chem. Soc. Rev.*, 2018, **47**, 2431–2453.
13 P.-B. Jin, K.-X. Yu, Q.-C. Luo, Y.-Y. Liu, Y.-Q. Zhai and Y.-Z. Zheng, Tetraanionic arachno-Carboranyl Ligand Imparts Strong Axiality to Terbium(III) Single-Molecule Magnets, *Angew. Chem., Int. Ed.*, 2022, **61**, e202203285.
14 P. Zhang, L. Zhang, C. Wang, S. Xue, S.-Y. Lin and J. Tang, Equatorially Coordinated Lanthanide Single Ion Magnets, *J. Am. Chem. Soc.*, 2014, **136**, 4484–4487.
15 A. J. Brown, D. Pinkowicz, M. R. Saber and K. R. Dunbar, A Trigonal-Pyramidal Erbium(III) Single-Molecule Magnet, *Angew. Chem., Int. Ed.*, 2015, **54**, 5864–5868.
16 J.-C. G. Bünzli, Lanthanide luminescence for biomedical analyses and imaging, *Chem. Rev.*, 2010, **110**, 2729–2755.
17 S. V. Eliseeva and J.-C. G. Bünzli, Lanthanide luminescence for functional materials and bio-sciences, *Chem. Soc. Rev.*, 2010, **39**, 189–227.
18 M. Hasegawa, H. Ohmagari, H. Tanaka and K. Machida, Luminescence of lanthanide complexes: From fundamental to prospective approaches related to water- and molecular-stimuli, *J. Photochem. Photobiol., C*, 2022, **50**, 100484.
19 L. D. Carlos, R. A. S. Ferreira, V. d. Z. Bermudez and S. J. L. Ribeiro, Lanthanide-Containing Light-Emitting Organic–Inorganic Hybrids: A Bet on the Future, *Adv. Mater.*, 2009, **21**, 509–534.
20 M. L. Langton, O. A. Blackburn, T. Lang, S. Faulkner and P. D. Beer, Nitrite-Templated Synthesis of Lanthanide-Containing [2]Rotaxanes for Anion Sensing, *Angew. Chem., Int. Ed.*, 2014, **53**, 11463–11466.
21 J. Zhou, H. Li, H. Zhang, H. Li, W. Shi and P. Cheng, A Bimetallic Lanthanide Metal-Organic Material as a Self-Calibrating Color-Gradient Luminescent Sensor, *Adv. Mater.*, 2015, **27**, 7072–7077.
22 L. E. MacKenzie and R. Pal, Circularly polarized lanthanide luminescence for advanced security inks, *Nat. Rev. Chem.*, 2021, **5**, 109–124.
23 A. J. Amoroso and S. J. A. Pope, Using lanthanide ions in molecular bioimaging, *Chem. Soc. Rev.*, 2015, **44**, 4723–4752.
24 X. Qiu, J. Xu, M. C. Dos Santos and N. Hildebrandt, Multiplexed Biosensing and Bioimaging Using Lanthanide-Based Time-Gated Förster Resonance Energy Transfer, *Acc. Chem. Res.*, 2022, **55**, 551–564.
25 T. Liang, Z. Guo, Y. He, Y. Wang, C. Li, Z. Li and Z. Liu, Cyanine-Doped Lanthanide Metal–Organic Frameworks for Near-Infrared II Bioimaging, *Adv. Sci.*, 2022, **9**, 2104561.
26 J.-H. Jia, Q.-W. Li, Y.-C. Chen, J.-L. Liu and M.-L. Tong, Luminescent single-molecule magnets based on lanthanides: Design strategies, recent advances and magneto-luminescent studies, *Coord. Chem. Rev.*, 2019, **378**, 365–381.
27 G. Cucinotta, M. Perfetti, J. Luzon, M. Etienne, P.-E. Car, A. Caneschi, G. Calvez, K. Bernot and R. Sessoli, Magnetic anisotropy in a dysprosium/DOTA single–molecule magnet: beyond simple magneto–structural correlations, *Angew. Chem., Int. Ed.*, 2012, **51**, 1606–1610.
28 F. Pointillart, B. Le Guennic, O. Cador, O. Maury and L. Ouahab, Lanthanide ion and tetrathiafulvalene-based ligand as a "magic" couple toward luminescence, single molecule magnets, and magnetostructural correlations, *Acc. Chem. Res.*, 2015, **48**, 2834–2842.
29 G. Brunet, R. Marin, M.-J. Monk, U. Resch-Genger, D. A. Gálico, F. A. Sigoli, E. A. Suturina, E. Hemmer and M. Murugesu, Exploring the dual functionality of an ytter-

bium complex for luminescence thermometry and slow magnetic relaxation, *Chem. Sci.*, 2019, **10**, 6799–6808.

30 R. Marin, G. Brunet and M. Murugesu, Shining new light on multifunctional lanthanide single–molecule magnets, *Angew. Chem., Int. Ed.*, 2021, **60**, 1728–1746.

31 S. Zanella, M. Aragon-Alberti, C. D. S. Brite, F. Salles, L. D. Carlos and J. Long, Luminescent Single–Molecule Magnets as Dual Magneto–Optical Molecular Thermometers, *Angew. Chem., Int. Ed.*, 2023, **62**, e202306970.

32 R. A. S. Ferreira, E. Mamontova, A. M. P. Botas, M. Shestakov, J. Vanacken, V. Moshchalkov, Y. Guari, L. F. Chibotaru, D. Luneau, P. A. Andre, J. Larionova, J. Long and L. D. Carlos, Synchronous Temperature and Magnetic Field Dual–Sensing by Luminescence in a Dysprosium Single–Molecule Magnet, *Adv. Opt. Mater.*, 2021, **9**, 2101495.

33 D. A. Galico and M. Murugesu, Toward Magneto–Optical Cryogenic Thermometers with High Sensitivity: A Magnetic Circular Dichroism Based Thermometric Approach, *Angew. Chem., Int. Ed.*, 2023, **62**, e202309152.

34 J. Corredoira-Vásquez, C. González-Barreira, A. M. Garcia-Deibe, J. Sanmartin-Matalobos, M. A. Hernandez-Rodriquez, C. D. S. Brites, L. D. Carlos and M. Fondo, Harnessing ligand design to develop primary and self-calibrated luminescent thermometers with field-induced single ion magnet behaviour in Dy^{3+} complexes, *Inorg. Chem. Front.*, 2024, **11**, 1087–1098.

35 Y. Bi, C. Chen, Y.-F. Zhao, Y.-Q. Zhang, S.-D. Jiang, B.-W. Wang, J.-B. Han, J.-L. Sun, Z.-Q. Bian, Z.-M. Wang and S. Gao, Thermostability and photoluminescence of Dy(III) single-molecule magnets under a magnetic field, *Chem. Sci.*, 2016, **7**, 5020–5031.

36 D. Errulat, R. Marin, D. A. Gálico, K. L. M. Harriman, A. Pialat, B. Gabidullin, F. Iikawa, O. D. D. Couto Jr., J. O. Moilanen, E. Hemmer, F. A. Sigoli and M. Murugesu, A luminescent thermometer exhibiting slow relaxation of the magnetization: toward self-monitored building blocks for next-generation optomagnetic devices, *ACS Cent. Sci.*, 2019, **5**, 1187–1198.

37 P. Ma, F. Hu, R. Wan, Y. Huo, D. Zhang, J. Niu and J. Wang, Magnetic double-tartaric bridging mono-lanthanide substituted phosphotungstates with photochromic and switchable luminescence properties, *J. Mater. Chem. C*, 2016, **4**, 5424–5433.

38 M. Hojorat, H. A. Sabea, L. Norel, K. Bernot, T. Roisnel, F. Gendron, B. Le Guennic, E. Trzop, E. Collet, J. R. Long and S. Rigaut, *J. Am. Chem. Soc.*, 2020, **142**, 931–936.

39 X.-D. Huang, X.-F. Ma and L.-M. Zheng, Hysteresis photomodulation via single-crystal-to-single-crystal isomerization of a photochromic chain of dysprosium single-molecule magnets, *Angew. Chem., Int. Ed.*, 2023, **62**, e202300088.

40 M.-J. Liu, Z.-Y. Fu, R. Sun, J. Yuan, C.-M. Liu, B. Zou, B.-W. Wang and H.-Z. Kou, Mechanochromic and single-molecule magnetic properties of a rhodamine 6G Dy(III) complex, *ACS Appl. Electron. Mater.*, 2021, **3**, 1368–1374.

41 Z. Zhu, C. Zhao, T. Feng, X. Liu, X. Ying, X.-L. Li, Y.-Q. Zhang and J. Tang, Air-stable chiral single-molecule magnets with record anisotropy barrier exceeding 1800 K, *J. Am. Chem. Soc.*, 2021, **143**, 10077–10082.

42 B. Lefeuvre, C. A. Mattei, J. F. Gonzalez, F. Gendron, V. Dorcet, F. Riobé, C. Lalli, B. Le Guennic, O. Cador, O. Maury, S. Guy, A. Bensalah-Ledoux, B. Baguenard and F. Pointillart, Solid–State Near–Infrared Circularly Polarized Luminescence from Chiral Yb^{III}–Single–Molecule Magnet, *Chem. – Eur. J.*, 2021, **27**, 7362–7366.

43 C. A. Mattei, V. Montigaud, V. Dorcet, F. Riobé, G. Argouarch, O. Maury, B. Le Guennic, O. Cador, C. Lalli and F. Pointillart, Luminescent dysprosium single-molecule magnets made from designed chiral BINOL-derived bisphosphate ligands, *Inorg. Chem. Front.*, 2021, **8**, 963–976.

44 S.-D. Zhu, J.-J. Hu, L. Dong, H.-R. Wen, S.-J. Liu, Y.-B. Lu and C.-M. Liu, Multifunctional Zn(II)–Yb(III) complex enantiomers showing second-harmonic generation, near-infrared luminescence, single-molecule magnet behaviour and proton conduction, *J. Mater. Chem. C*, 2020, **8**, 16032–16041.

45 J. Long, M. S. Ivanov, V. A. Khomchenko, E. Mamontova, J.-M. Thibaud, J. Rouquette, M. Beaudhuin, D. Granier, R. A. S. Ferreira, L. D. Carlos, B. Donnadieu, M. S. C. Henriques, J. A. Paixão, Y. Guari and J. Larionova, Room temperature magnetoelectric coupling in a molecular ferroelectric ytterbium(III) complex, *Science*, 2020, **367**, 671–676.

46 T. Sato, B. K. Breedlove, M. Yamashita and K. Katoh, Electro–Conductive Single–Molecule Magnet Composed of a Dysprosium(III)–Phthalocyaninato Double–Decker Complex with Magnetoresistance, *Angew. Chem., Int. Ed.*, 2021, **60**, 21179–21183.

47 C. Train, R. Gheorghe, V. Krstic, L.-M. Chamoreau, N. S. Ovanesyan, G. L. J. A. Rikken, M. Gruselle and M. Verdaguer, Strong magneto-chiral dichroism in enantiopure chiral ferromagnets, *Nat. Mater.*, 2008, **7**, 729–734.

48 R. Sessoli, M.-E. Boulon, A. Caneschi, M. Mannini, L. Poggini, F. Wilhelm and A. Rogalev, Strong magneto-chiral dichroism in a paramagnetic molecular helix observed by hard X-rays, *Nat. Phys.*, 2015, **11**, 69–74.

49 M. Atzori, F. Santanni, I. Breslavetz, K. Paillot, A. Caneschi, G. L. J. A. Rikken, R. Sessoli and C. Train, Magnetic anisotropy drives magnetochiral dichroism in a chiral molecular helix probed with visible light, *J. Am. Chem. Soc.*, 2020, **142**, 13908–13916.

50 X.-D. Huang, Y. Xu, K. Fan, S.-S. Bao, M. Kurmoo and L.-M. Zheng, Reversible SC–SC Transformation involving [4 + 4] Cycloaddition of Anthracene: A Single–Ion to Single–Molecule Magnet and Yellow–Green to Blue–White Emission, *Angew. Chem., Int. Ed.*, 2018, **57**, 8577–8581.

51 X.-D. Huang, J.-G. Jia, M. Kurmoo, S.-S. Bao and L.-M. Zheng, Interplay of anthracene luminescence and dysprosium magnetism by steric control of photodimerization, *Dalton Trans.*, 2019, **48**, 13769–13779.

52 X.-D. Huang, G.-H. Wen, S.-S. Bao, J.-G. Jia and L.-M. Zheng, Thermo- and light-triggered reversible interconversion of dysprosium–anthracene complexes and their responsive optical, magnetic and dielectric properties, *Chem. Sci.*, 2021, **12**, 929–937.

53 S.-D. Jiang, B.-W. Wang, G. Su, Z.-M. Wang and S. Gao, A Mononuclear Dysprosium Complex Featuring Single–Molecule–Magnet Behavior, *Angew. Chem., Int. Ed.*, 2010, **49**, 7448–7451.

54 X. Yi, K. Bernot, F. Pointillart, G. Poneti, G. Calvez, C. Daiguebonne, O. Guillou and R. Sessoli, A Luminescent and Sublimable Dy^{III}–Based Single–Molecule Magnet, *Chem. – Eur. J.*, 2012, **18**, 11379–11387.

55 F. Pointillart, B. Le Guennic, S. Golhen, O. Cador, O. Maury and L. Ouahab, A redox-active luminescent ytterbium based single molecule magnet, *Chem. Commun.*, 2013, **49**, 615–617.

56 M. Menelaou, F. Ouharrou, L. Rodríguez, O. Roubeau, S. J. Teat and N. Aliaga-Alcalde, Dy(III)- and Yb(III)-curcuminoid compounds: original fluorescent single-ion magnet and magnetic near-IR luminescent species, *Chem. – Eur. J.*, 2012, **18**, 11545–11549.

57 D. A. Gálico, R. Marin, G. Brunet, D. Errulat, E. Hemmer, F. A. Sigoli, J. O. Moilanen and M. Murugesu, Triplet–State Position and Crystal–Field Tuning in Opto–Magnetic Lanthanide Complexes: Two Sides of the Same Coin, *Chem. – Eur. J.*, 2019, **25**, 14625–14637.

58 S. Chorazy, M. Rams, K. Nakabayashi, B. Sieklucka and S. Ohkoshi, White Light Emissive DyIII Single–Molecule Magnets Sensitized by Diamagnetic $[Co^{III}(CN)_6]^{3-}$ Linkers, *Chem. – Eur. J.*, 2016, **22**, 7371–7375.

59 J. J. Zakrzewski, S. Chorazy, K. Nakabayashi, S. Ohkoshi and B. Sieklucka, Photoluminescent Lanthanide (III) Single–Molecule Magnets in Three–Dimensional Polycyanidocuprate (I)–Based Frameworks, *Chem. – Eur. J.*, 2019, **25**, 11820–11825.

60 Y. Liu, Y.-C. Chen, J. Liu, W.-B. Chen, G.-Z. Huang, S.-G. Wu, J. Wang, J.-L. Liu and M.-L. Tong, Cyanometallate-bridged didysprosium single-molecule magnets constructed with single-ion magnet building block, *Inorg. Chem.*, 2020, **59**, 687–694.

61 S. Chorazy, J. J. Zakrzewski, M. Reczyński, K. Nakabayashi, S. Ohkoshi and B. Sieklucka, Humidity driven molecular switch based on photoluminescent $Dy^{III}Co^{III}$ single-molecule magnets, *J. Mater. Chem. C*, 2019, **7**, 4164–4172.

62 Y. Xin, J. Wang, M. Zychowicz, J. J. Zakrzewski, K. Nakabayashi, B. Sieklucka, S. Chorazy and S. Ohkoshi, Dehydration–Hydration Switching of Single-Molecule Magnet Behavior and Visible Photoluminescence in a Cyanido-Bridged $Dy^{III}Co^{III}$ Framework, *J. Am. Chem. Soc.*, 2019, **141**, 18211–18220.

63 J. Wang, J. J. Zakrzewski, M. Heczko, M. Zychowicz, K. Nakagawa, K. Nakabayashi, B. Sieklucka, S. Chorazy and S. Ohkoshi, Proton Conductive Luminescent Thermometer Based on Near-Infrared Emissive $\{YbCo_2\}$ Molecular Nanomagnets, *J. Am. Chem. Soc.*, 2020, **142**, 3970–3979.

64 J. Wang, J. J. Zakrzewski, M. Zychowicz, V. Vieru, L. F. Chibotaru, K. Nakabayashi, S. Chorazy and S. Ohkoshi, Holmium(III) molecular nanomagnets for optical thermometry exploring the luminescence re-absorption effect, *Chem. Sci.*, 2021, **12**, 730–741.

65 M. Wyczesany, J. J. Zakrzewski, B. Sieklucka and S. Chorazy, Metal-cyanido molecular modulators of the sensing range and performance in lanthanide-based luminescent thermometers, *J. Mater. Chem. C*, 2022, **10**, 12054–12069.

66 J. Wang, J. J. Zakrzewski, M. Zychowicz, Y. Xin, H. Tokoro, S. Chorazy and S. Ohkoshi, Desolvation–Induced Highly Symmetrical Terbium(III) Single–Molecule Magnet Exhibiting Luminescent Self–Monitoring of Temperature, *Angew. Chem., Int. Ed.*, 2023, **62**, e202306372.

67 J. Forniés, S. Fuertes, J. A. López, A. Martín and V. Sicilia, New Water Soluble and Luminescent Platinum(II) Compounds, Vapochromic Behavior of $[K(H_2O)][Pt(bzq)(CN)_2]$, New Examples of the Influence of the Counterion on the Photophysical Properties of d^8 Square-Planar Complexes, *Inorg. Chem.*, 2008, **47**, 7166–7176.

68 A. F. Rausch, U. V. Monkowius, M. Zabel and H. Yersin, Bright Sky-Blue Phosphorescence of $[n\text{-}Bu_4N][Pt(4,6\text{-}dFppy)(CN)_2]$: Synthesis, Crystal Structure, and Detailed Photophysical Studies, *Inorg. Chem.*, 2010, **49**, 7818–7825.

69 B. D. Belviso, F. Marin, S. Fuertes, V. Sicilia, R. Rizzi, F. Ciriaco, C. Cappuccino, E. Dooryhee, A. Falcicchio, L. Maini, A. Altomare and R. Caliandro, Structural insights into the vapochromic behavior of Pt-and Pd-based compounds, *Inorg. Chem.*, 2021, **60**, 6349–6366.

70 J. Li, K. Chen, J. Wei, Y. Ma, R. Zhou, S. Liu, Q. Zhao and W.-Y. Wong, Reversible on–off switching of excitation-wavelength-dependent emission of a phosphorescent soft salt based on platinum(II) complexes, *J. Am. Chem. Soc.*, 2021, **143**, 18317–18324.

71 M. Liberka, M. Zychowicz, M. Zychowicz and S. Chorazy, Neutral dicyanidoferrate (II) metalloligands for the rational design of dysprosium(III) single-molecule magnets, *Chem. Commun.*, 2022, **58**, 6381–6384.

72 M. Llunell, D. Casanova, J. Cirera, J. Bofill, P. Alemany, S. Alvarez, M. Pinsky and D. Avnir, *SHAPE v. 2.1. Program for the Calculation of Continuous Shape Measures of Polygonal and Polyhedral Molecular Fragments*, University of Barcelona, Barcelona, Spain, 2013.

73 D. Casanova, J. Cirera, M. Llunell, P. Alemany, D. Avnir and S. Alvarez, Minimal distortion pathways in polyhedral rearrangements, *J. Am. Chem. Soc.*, 2004, **126**, 1755–1763.

74 P. Beak and J. Bonham, The Deuteration of Some N-Methyl-4-pyridones, *J. Am. Chem. Soc.*, 1965, **87**, 3365–3371.

75 G. S.-M. Tong and C.-M. Che, Emissive or nonemissive? A theoretical analysis of the phosphorescence efficiencies of cyclometalated platinum(II) complexes, *Chem. – Eur. J.*, 2009, **15**, 7225–7237.

76 A. M. Prokhorov, T. Hofbeck, R. Czerwieniec, A. F. Suleymanova, D. N. Kozhevnikov and H. Yersin,

Brightly luminescent Pt(II) pincer complexes with a sterically demanding carboranyl-phenylpyridine ligand: a new material class for diverse optoelectronic applications, *J. Am. Chem. Soc.*, 2014, **136**, 9637–9642.

77 A. Díez, J. Forniés, C. Larraz, E. Lalinde, J. A. López, A. Martín, M. T. Moreno and V. Sicilia, Structural and luminescence studies on π··· π and Pt··· Pt interactions in mixed chloro-isocyanide cyclometalated platinum(II) complexes, *Inorg. Chem.*, 2010, **49**, 3239–3251.

78 A. Díez, J. Forniés, S. Fuertes, E. Lalinde, C. Larraz, J. A. López, A. Martín, M. T. Moreno and V. Sicilia, Synthesis and luminescence of cyclometalated compounds with nitrile and isocyanide ligands, *Organometallics*, 2009, **28**, 1705–1718.

79 C. F. R. Mackenzie, S.-Y. Kwak, S. Kim and E. Zysman-Colman, The design and synthesis of green emissive iridium(III) complexes guided by calculations of the vibrationally-resolved emission spectra, *Dalton Trans.*, 2023, **53**, 4112–4121.

80 F. Egidi, M. Fusè, A. Baiardi, J. Bloino, X. Li and V. Barone, Computational simulation of vibrationally resolved spectra for spin–forbidden transitions, *Chirality*, 2018, **30**, 850–865.

81 S. Chorazy, J. J. Zakrzewski, J. Wang, S. Ohkoshi and B. Sieklucka, Incorporation of hexacyanidoferrate(III) ion in photoluminescent trimetallic Eu(3-pyridone) $[Co_{1-x}Fe_x(CN)_6]$ chains exhibiting tunable visible light absorption and emission properties, *CrystEngComm*, 2018, **20**, 5695–5706.

82 J. Rocha, C. D. S. Brites and L. D. Carlos, Lanthanide organic framework luminescent thermometers, *Chem. – Eur. J.*, 2016, **22**, 14782–14795.

83 C. D. S. Brites, R. Marin, M. Suta, A. N. C. Neto, E. Ximedes, D. Jaque and L. D. Carlos, Spotlight on luminescence thermometry: basics, challenges, and cutting–edge applications, *Adv. Mater.*, 2023, **35**, 2302749.

84 B. O. Roos, R. Lindh, P.-Å. Malmqvist, V. Veryazov and P.-O. Widmark, Main group atoms and dimers studied with a new relativistic ANO basis set, *J. Phys. Chem. A*, 2004, **108**, 2851–2858.

85 B. O. Roos, R. Lindh, P.-Å. Malmqvist, V. Veryazov and P.-O. Widmark, New relativistic ANO basis sets for transition metal atoms, *J. Phys. Chem. A*, 2005, **109**, 6575–6579.

86 B. O. Roos, R. Lindh, P.-A. Malmqvist, V. Veryazov, P.-O. Widmark and A. C. Borin, New Relativistic Atomic Natural Orbital Basis Sets for Lanthanide Atoms with Applications to the Ce Diatom and LuF_3, *J. Phys. Chem. A*, 2008, **112**, 11431–11435.

87 P.-Å. Malmqvist, B. O. Roos and B. Schimmelpfennig, The restricted active space (RAS) state interaction approach with spin–orbit coupling, *Chem. Phys. Lett.*, 2002, **357**, 230–240.

88 B. A. Heß, C. M. Marian, U. Wahlgren and O. Gropen, A mean-field spin-orbit method applicable to correlated wavefunctions, *Chem. Phys. Lett.*, 1996, **251**, 365–371.

89 L. F. Chibotaru and L. Ungur, *Ab initio* calculation of anisotropic magnetic properties of complexes. I. Unique definition of pseudospin Hamiltonians and their derivation, *J. Chem. Phys.*, 2012, **137**, 064112.

90 L. Ungur and L. F. Chibotaru, Ab initio calculation of anisotropic magnetic properties of complexes. I. Unique definition of pseudospin Hamiltonians and their derivation, *Chem. – Eur. J.*, 2017, **23**, 3708–3718.

91 Y.-N. Guo, G.-F. Xu, Y. Guo and J. Tang, Relaxation dynamics of dysprosium(III) single molecule magnets, *Dalton Trans.*, 2011, **40**, 9953–9963.

92 S. T. Liddle and J. van Slageren, Improving f-element single molecule magnets, *Chem. Soc. Rev.*, 2015, **44**, 6655–6669.

93 D. Errulat, K. L. M. Harriman, D. A. Gálico, A. A. Kitos, A. Mansikkamäki and M. Murugesu, A trivalent 4f complex with two bis-silylamide ligands displaying slow magnetic relaxation, *Nat. Chem.*, 2023, **15**, 1100–1107.

94 D. Maniaki, P. S. Perlepe, E. Pilichos, S. Christodoulou, M. Rouzières, P. Dechambenoit, R. Clérac and S. P. Perlepes, Asymmetric Dinuclear Lanthanide(III) Complexes from the Use of a Ligand Derived from 2-Acetylpyridine and Picolinoylhydrazide: Synthetic, Structural and Magnetic Studies, *Molecules*, 2020, **25**, 3153.

